

Enhanced Sulfur and Coking Tolerance of a Mixed Ion Conductor for SOFCs: $\text{BaZr}_{0.1}\text{Ce}_{0.7}\text{Y}_{0.2-x}\text{Yb}_x\text{O}_{3-\delta}$

Lei Yang, Shizhong Wang, Kevin Blinn, Mingfei Liu, Ze Liu, Zhe Cheng, Meilin Liu*

The anode materials that have been developed for solid oxide fuel cells (SOFCs) are vulnerable to deactivation by carbon buildup (coking) from hydrocarbon fuels or by sulfur contamination (poisoning). We report on a mixed ion conductor, $\text{BaZr}_{0.1}\text{Ce}_{0.7}\text{Y}_{0.2-x}\text{Yb}_x\text{O}_{3-\delta}$, that allows rapid transport of both protons and oxide ion vacancies. It exhibits high ionic conductivity at relatively low temperatures (500° to 700°C). Its ability to resist deactivation by sulfur and coking appears linked to the mixed conductor's enhanced catalytic activity for sulfur oxidation and hydrocarbon cracking and reforming, as well as enhanced water adsorption capability.

Unlike polymer electrolyte fuel cells, solid oxide fuel cells (SOFCs) can use a wide variety of hydrocarbon fuels (1). Because of their high operating temperatures (600° to 800° C), metal catalysts added to the ceramic anodes can facilitate reforming reactions that generate H_2 and CO from hydrocarbons. The conventional anode for a SOFC, a composite consisting of nickel and yttria-stabilized zirconia (YSZ), has excellent catalytic activity for fuel oxidation, good conductivity for current collection, and unmatched compatibility with YSZ electrolyte for easy cell fabrication, but it is highly susceptible to carbon buildup (coking) and deactivation (poisoning) by contaminants commonly encountered in readily available fuels (2). Some contaminants (e.g., sulfur impurities) can degrade its performance even at parts per million (ppm) levels (3). Sulfur ad-

sorbs strongly on Ni surface and thus blocks the active sites for electrochemical oxidation of fuel, resulting in considerably increased anodic polarization and energy loss.

To overcome these problems, substantial effort has been devoted to the development of new anode materials and novel electrode structures (4–11). For example, the use of ceria-based anodes demonstrated the potential for direct use of methane in a SOFC (4). Later, the use of a composite anode consisting of copper and ceria led to successful operation of a SOFC with higher hydrocarbons than methane, which are more prone to coking because of their higher carbon content (5). However, some practical issues still remain: The low melting point of Cu makes it difficult to fabricate anode-supported cells using conventional co-firing ceramic methods, and the poor catalytic activity of Cu for fuel oxidation limits cell power output. In another approach, a catalyst layer (e.g., Ru-ceria) was applied to a conventional Ni-YSZ anode to allow internal reforming of hydrocarbons. The ef-

fectiveness of this cell structure was confirmed for direct use of iso-octane without coking in a SOFC with power densities of 0.3 to 0.6 W/cm^2 at 670° to 770°C (7). Although this cell design has demonstrated the possibility of a simple low-cost SOFC system with common automotive fuels, the drawbacks include decreased power density, difficulty in current collection, and the high cost of Ru.

Nickel-free conducting metal oxides have also been developed as anode materials, including $\text{La}_{0.75}\text{Sr}_{0.25}\text{Cr}_{0.5}\text{Mn}_{0.5}\text{O}_{3-\delta}$ (with a $\text{Ce}_{0.8}\text{Gd}_{0.2}\text{O}_{2-\delta}$ interlayer) (6), $\text{Sr}_2\text{Mg}_{1-x}\text{Mn}_x\text{MoO}_{6-\delta}$ ($x = 0$ to 1) (9), and doped (La,Sr)(Ti)O₃ (8, 11). These anode materials showed different degrees of improved tolerance to coking, reoxidation, and/or sulfur poisoning under various SOFC operating conditions. In many cases, however, the power densities of the SOFCs using Ni-free oxide anodes are less than those demonstrated by conventional Ni-YSZ-supported SOFCs with thin electrolytes (by more than 50%). This low efficiency arises from difficulties in fabricating thin-YSZ electrolyte on porous oxide anode supports that arise from delamination or formation of undesirable phases. In some cases, inadequate lateral conductivity (or substantial sheet resistance) of Ni-free oxide anodes also contributes to low power density, especially for SOFC designs with long current collection paths, as in fuel cell stacks.

To compensate for these issues, conducting oxides (e.g., $\text{Sr}_{0.8}\text{La}_{0.2}\text{TiO}_3$) have been used as anode-side supports together with an interlayer (e.g., a ceramic-metal composite, or cermet, of Ni and doped ceria) to allow fabrication of an anode-supported thin-electrolyte SOFC via conventional ceramic processing methods (12). This cell design leads to high power densities, much-improved stability against coking in natural gas, and enhanced tolerance to H_2S poisoning.

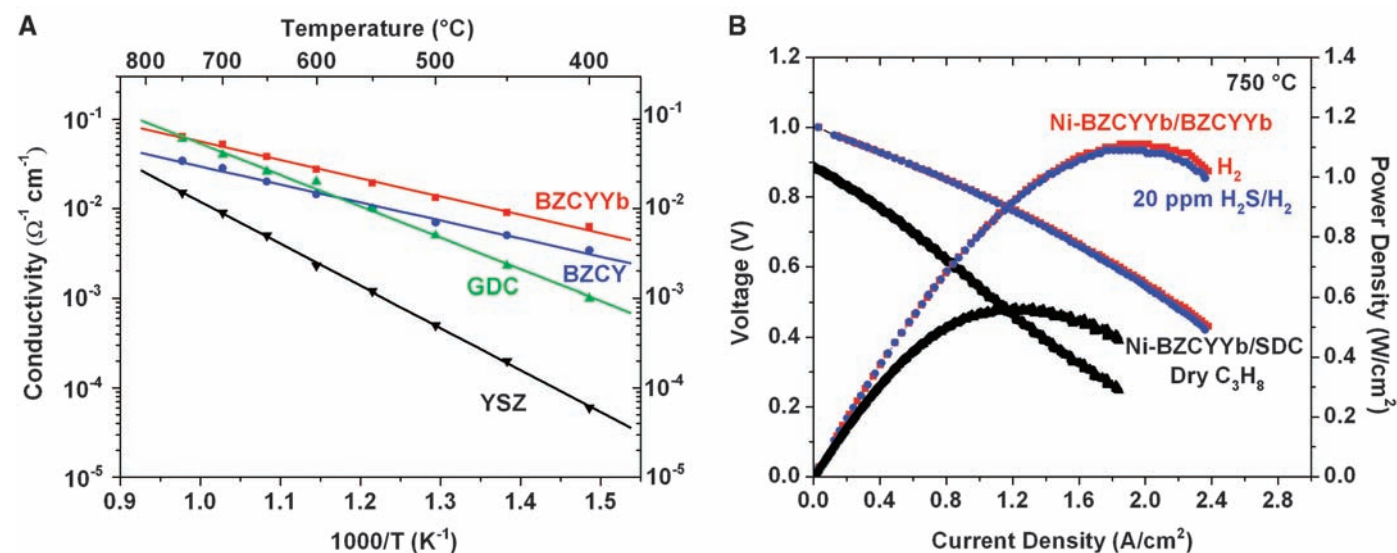


Fig. 1. (A) Ionic conductivities of BZCYYb, BZCY, GDC, and YSZ as measured at 400° to 750°C in wet oxygen (with ~3 vol % H_2O). (B) Typical current-voltage characteristics and the corresponding power densities measured at 750°C for a cell with a configuration of Ni-BZCYYb | BZCYYb |

BZCY-LSCF when ambient air was used as oxidant and hydrogen as fuel (with or without 20 ppm H_2S contamination), and for another cell with a configuration of Ni-BZCYYb | SDC | LSCF when dry propane was used as fuel.

Alternative anode materials and innovative anode structures have improved the tolerance to coking and poisoning by contaminants. To date, however, an initial drop of substantial magnitude in power output upon exposure to H₂S-contaminated fuels still appears unavoidable for any known anode materials. For example, the power output of a cell with Sr_{0.8}La_{0.2}TiO₃ as the anode-side support (which represents the latest advance in development of sulfur-tolerant anodes) dropped ~19% upon exposure to 100 ppm H₂S/H₂, although there was no additional degradation in performance under steady-state operation and the performance was fully recovered upon removal of H₂S (12).

We report high tolerance to coking and H₂S poisoning of a new material for SOFCs, a barium zirconate-cerate codoped with Y and Yb: BaZr_{0.1}Ce_{0.7}Y_{0.1}Yb_{0.1}O_{3-δ} (BZCYYb). This material has very high ionic conductivity below 750°C (Fig. 1A), which allows for fabri-

cation of anode-supported thin-electrolyte SOFCs of high power output at lower temperatures. There is no observable change in power output when the fuel is switched to one contaminated with 50 ppm H₂S, which we attributed to catalytic conversion of H₂S to SO₂. Moreover, continuous and stable operation in dry propane for more than 100 hours without observable degradation in performance suggests that it is very effective for in situ reformation of hydrocarbons, which should help inhibit coking. Finally, it demonstrates adequate chemical and electrochemical stability over a wide range of conditions relevant to SOFC operation, implying long-term stability and long operational life. We also systematically investigated anodes consisting of Ni and BZCYYb in H₂S-contaminated H₂ and hydrocarbon fuels. They displayed not only impressive power output in clean hydrogen but also superior tolerance to coking and sulfur poisoning.

Doped zirconate-cerate compounds have been reported to exhibit both proton and oxide ion conductivity as well as a strong tendency for water absorption (or hydration) (13–17). For example, Y-doped zirconate-cerate, Ba(Zr_{0.1}Ce_{0.7}Y_{0.2})O_{3-δ} (BZCY), has high ionic conductivity and excellent chemical stability in atmospheres containing CO₂ and H₂O under SOFC operating conditions (18). Here, we explored codoping barium zirconate-cerate with Y and Yb using compositions of BaZr_{0.1}Ce_{0.7}Y_{0.2-x}Yb_xO_{3-δ} (x = 0 to 0.2). We believe that the two dopants on the B-site function in a cooperative fashion to improve the ionic conductivity and the catalytic activity for reforming or oxidation of hydrocarbons as well as conversion of H₂S to SO₂.

When we compared the conductivities of BZCYYb with those of several other SOFC electrolyte materials, namely YSZ, GDC, and BZCY (Fig. 1A), BZCYYb displayed the highest conductivity below 750°C. Operation of SOFCs

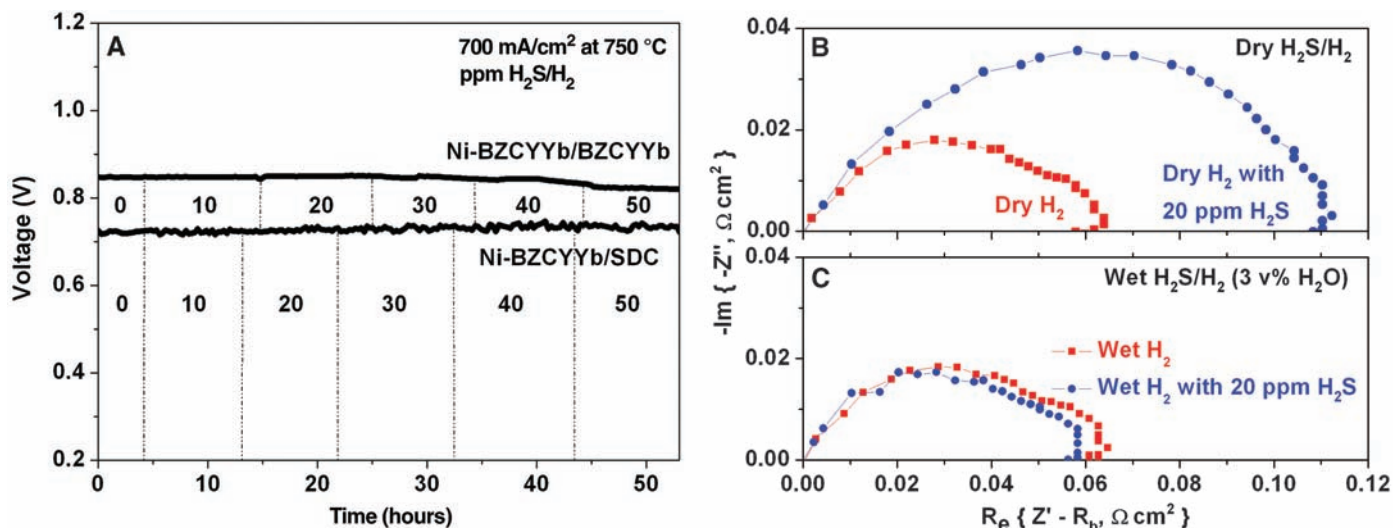


Fig. 2. (A) Terminal voltages measured at 750°C as a function of time for two cells with a configuration of Ni-BZCYYb | BZCYYb | BZCY-LSCF and Ni-BZCYYb | SDC | LSCF operated at a constant current density of 700 mA/cm² as the fuel was switched from clean H₂ to H₂ contaminated with different concentrations of H₂S (the number in each time interval represents

the concentration of H₂S in wet hydrogen in ppm). (B and C) Impedance spectra measured under OCV conditions at 750°C for a cell with a configuration of Ni-BZCYYb | SDC | LSCF in clean H₂ and in H₂ contaminated with 20 ppm H₂S for dry H₂/H₂ gases (B) and wet H₂/H₂ gases (with ~3 vol % H₂O) (C).

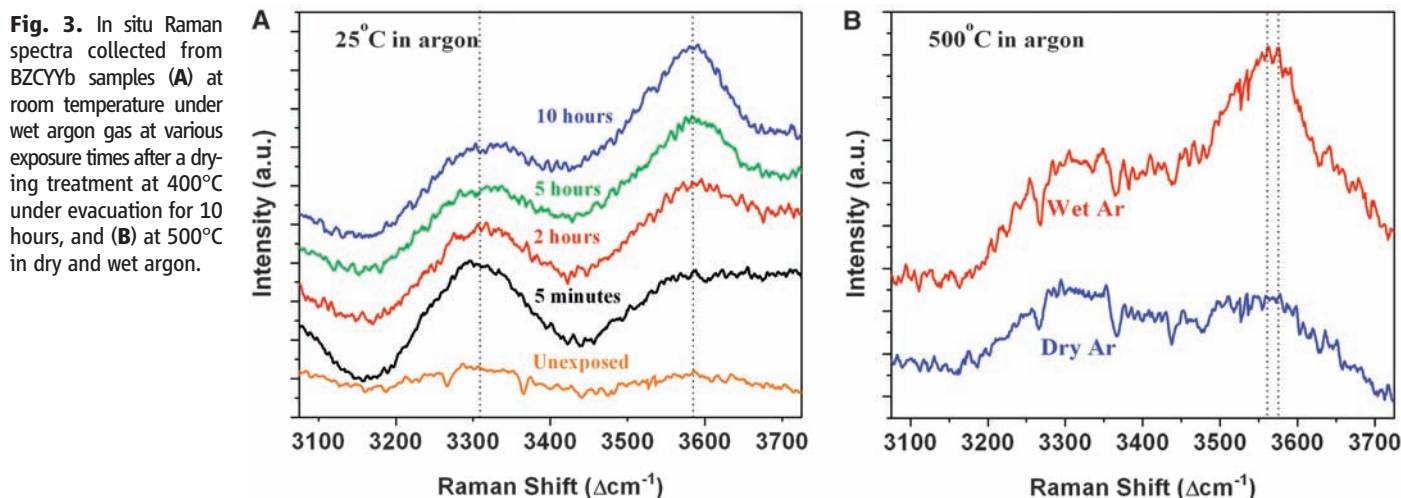
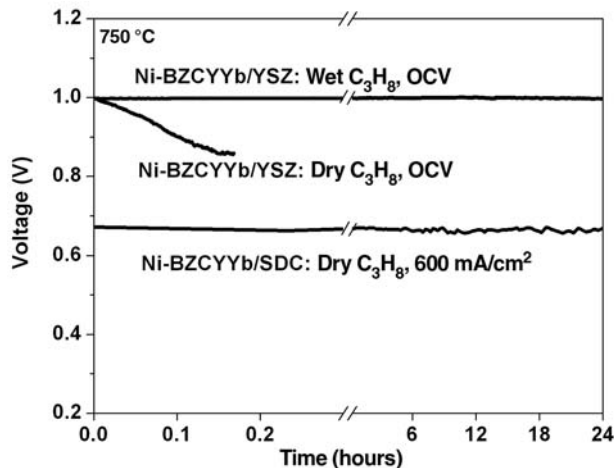


Fig. 3. In situ Raman spectra collected from BZCYYb samples (A) at room temperature under wet argon gas at various exposure times after a drying treatment at 400°C under evacuation for 10 hours, and (B) at 500°C in dry and wet argon.

at lower temperatures makes it possible to use much less expensive materials for cell components, thus reducing the cost while prolonging the operational life. As expected, the conductivities are sensitive to doping and partial pressure of oxygen, hydrogen, and water (figs. S1 and S2). When used as the electrolyte in a SOFC, the electronic conductivity of BZCYYb is relatively small, more so at lower temperatures (fig. S3). When used as a component for the anode and exposed to hydrogen and water, however, not only the ionic defects ($\text{OH}_\text{O}^\bullet$ and $\text{V}_\text{O}^{\bullet\bullet}$) but also the electronic defects (e^- and h^+) may coexist, enhancing the catalytic activity for reforming and/or oxidation of hydrocarbons and for conversion of H_2S to SO_2 . Although the conductivity of BZCYYb is about 80% better than that of BZCY (at 750°C), the catalytic activities of BZCYYb are quite different from that of BZCY. Under open circuit conditions, for example, the cells with a Ni-BZCYYb anode show higher and more stable open cell voltages (OCVs) than the cells with a Ni-BZCY anode when exposed to wet propane at 750°C (fig. S4), an indication of much-improved ability of hydrocarbon reformation.

Typical performance of a cell based on a Ni-BZCYYb cermet anode, a BZCYYb electrolyte, and a composite cathode consisting of BZCY and LSCF (19) (fig. S5) entailed peak power densities of $\sim 1.1 \text{ W/cm}^2$ at 750°C (Fig. 1B) and $\sim 660 \text{ mW/cm}^2$ at 650°C (fig. S6) when H_2 and ambient air were used as fuel and oxidant, respectively. Further, when the fuel was switched to H_2 contaminated with 20 ppm H_2S , the observed power output remained about the same. Moreover, a cell based on a Ni-BZCYYb anode and a $\text{Sm}_{0.1}\text{Ce}_{0.9}\text{O}_{2-\delta}$ (SDC) electrolyte displayed a peak power density of 564 mW/cm^2 at 750°C when dry propane was used as the fuel, showing a considerably high resistance to coking and power output for a SOFC running on dry hydrocarbon. Typically, water has to be fed with a hydrocarbon fuel to prevent coking; however, addition of water will reduce the energy efficiency while increasing the complexity and cost of fuel cell systems (because it dilutes the fuel and requires a water management subsystem).

Fig. 4. Open cell voltages measured at 750°C as a function of time for a cell with a configuration of Ni-BZCYYb | YSZ | LSCF with dry and wet propane as the fuel, and the terminal voltages for another cell with a configuration of Ni-BZCYYb | SDC | LSCF operated at 600 mA/cm^2 using dry propane as fuel. Stationary air was used as oxidant in all cases.



We investigated the sensitivity of this anode to sulfur poisoning by gradually increasing the concentration of H_2S in hydrogen. The terminal voltages of the same cells (with BZCYYb and SDC as the electrolyte) at 750°C were recorded as a function of time when the fuel was contaminated with different concentrations of H_2S (Fig. 2A). The Ni-BZCYYb anodes for both cells showed no observable change in power output as the fuel was switched from clean hydrogen to hydrogen contaminated with 10, 20, or 30 ppm H_2S . This sulfur tolerance was also evident from our impedance data (Fig. 2, B and C). When water was absent from the fuel, the electrode polarization resistance increased about 80% upon exposure to 20 ppm H_2S , from $\sim 0.06 \text{ ohm}\cdot\text{cm}^2$ in H_2 to $\sim 0.11 \text{ ohm}\cdot\text{cm}^2$ in H_2 containing 20 ppm H_2S , as commonly observed in previous studies (20). When a small amount of water (only $\sim 3 \text{ vol } \%$) was introduced with the fuel, the electrode polarization resistance in hydrogen with 20 ppm H_2S was reduced to that in clean hydrogen, as can be interpreted from the collected impedance spectra (Fig. 2C). It is believed that sulfur poisoning is caused by the strong adsorption of the elemental sulfur on Ni surface and the three-phase boundaries (TPBs) between Ni, electrolyte, and the fuel. Sulfur would then block the active site for fuel oxidation in a traditional Ni-YSZ anode and increase the polarization resistance (21, 22). We hypothesized that water might adsorb on the surface of BZCYYb to facilitate the oxidation of H_2S or elemental sulfur to SO_2 at or near the active sites. Unlike H_2S or elemental sulfur, SO_2 readily desorbs from electrode surface (23).

When the fuel was switched to hydrogen containing 40 and 50 ppm H_2S , the cell with a BZCYYb electrolyte (a mixed proton and oxide ion conductor) suffered some drop in power output, whereas the cell with an SDC electrolyte (an oxide ion conductor) displayed no observable change in performance. One possible explanation is that more water was produced at the active sites on the anode of the cell with an SDC electrolyte under active operation because of increased hydrogen oxidation; the water produced at the

active sites is beneficial to sulfur removal. Continuous operation in H_2S -contaminated fuel for a longer period of time (200 to 1000 hours) further confirmed that sulfur poisoning can be fully suppressed in the presence of a small amount of steam (figs. S7 and S8).

We used Raman spectroscopy to probe for the presence of water on the surface of BZCYYb. Previous studies suggest that the characteristic OH-bond vibration modes for water appear in the 3100 to 3700 cm^{-1} regime (24, 25). We collected Raman spectra from BZCYYb at different times of exposure to wet argon ($\sim 3 \text{ vol } \%$ water) at room temperature, where incorporation of water into the bulk phase of BZCYYb is unlikely or negligible because of limited bulk diffusion. The BZCYYb powder sample was first dried at 400°C under evacuation for 10 hours to remove water from the sample. Upon exposure to wet ($3 \text{ vol } \%$ H_2O) argon at room temperature, the mode near 3580 cm^{-1} emerged and slowly grew more intense over time. The presence of the modes in the 3100 to 3700 cm^{-1} range, particularly the mode that peaks near 3580 cm^{-1} (Fig. 3A), is strongly indicative of surface water molecules, as water modes at higher wavenumbers may correspond to adsorbed water with weak hydrogen bonds (26). Thus, one possible explanation for this behavior is that an initial layer of water accumulates at the surface quickly in a wet atmosphere, whereas any further water that adsorbs onto this layer builds up more slowly. These features are notably absent from the sample exposed to dry gas. Spectra collected in situ from samples held under the same gas conditions at 500°C display similar features and contrast (Fig. 3B). Because most fuels (including H_2) are humidified at room temperature (yielding $\sim 3 \text{ vol } \%$ H_2O in gas) for typical operation of SOFCs, no excess water is needed to achieve the desired tolerance to H_2S contaminants.

The coking resistance of this material was demonstrated in a cell with a Ni-BZCYYb cermet anode, YSZ electrolyte, and LSCF cathode. When dry propane was used as fuel, the OCV dropped quickly within minutes (Fig. 4), an indication of rapid carbon deposition as expected for a conventional Ni-based anode. In contrast, when wet ($\sim 3 \text{ vol } \%$ steam) propane was used as fuel, the OCV was very stable (Fig. 4), suggesting that the observed tolerance to coking is also attributed to the presence of a small amount of steam. Further, the contamination of Ni surface by BZCYYb during co-firing of BZCYYb and NiO might enhance the resistance to carbon buildup (fig. S9). The whole surface of the Ni-BZCYYb anode exposed to wet ($\sim 3 \text{ vol } \%$ H_2O) propane appeared clean and free of carbon deposition, as revealed by Raman spectroscopy (fig. S10). The OCVs of the cell are greater than those observed for other alternative anode materials (5, 6, 9, 27) and approach 1.00 V for wet propane. Coking may be inhibited by water reforming propane on the surface of BZCYYb, and the reforming products (H_2 and

CO) adsorb on the active sites of the anode surface, leading to a stable OCV output. We note that conventional Ni-YSZ and Ni-GDC anodes suffered severe carbon deposition under the same conditions (fig. S11).

This catalytic activity of Ni-BZCYYb in situ reforming of hydrocarbons was further demonstrated in operating cells powered by propane. A stable power output was observed for more than 100 hours (fig. S12) at a current density of 300 mA/cm² for a cell with a Ni-BZCYYb anode, a YSZ electrolyte, and an LSCF cathode when wet (~3 vol % steam) propane was used as fuel and air as oxidant. Analysis of the effluent gas by mass spectrometry indicated that propane was mostly converted to C₂H₄, CH₄, H₂, H₂O, CO₂, and CO through cracking, reformation, and electrochemical oxidation during cell operation (fig. S13). In contrast, conventional Ni-YSZ anodes studied under similar conditions showed rapid degradation in performance within minutes as a result of severe carbon deposition.

Because steam is produced on the anode surface of an operating cell when an oxygen anion conductor (e.g., SDC) is used as the electrolyte, tolerance to coking of BZCYYb-based anodes may be further enhanced by an operating current of such a fuel cell. Indeed, when the operating current density is sufficiently high, cells based on an SDC electrolyte (Fig. 4) can even operate in dry propane, producing stable power output without observable degradation. Microanalysis of the anode before and after operation in dry propane for 24 hours indicates that there was no visible change in microstructure and no observable carbon deposition (fig. S14). It appears that in situ reformation of hydrocarbons has prevented carbon deposition on the anode when an adequate

amount of water is produced at the active sites under the operating conditions.

To examine the chemical stability, we exposed BZCYYb powder samples to H₂ containing 50 vol % CO₂ or 50 vol % H₂O at 750°C for 300 hours and to H₂ containing 50 ppm H₂S at 750°C for 50 hours. X-ray diffraction (XRD) analysis of the samples before and after the exposures confirmed that BZCYYb is chemically stable under these testing conditions (figs. S15 and S16). Raman spectra were also collected from BZCYYb powder samples under wet and dry conditions in the 100 to 1000 cm⁻¹ range in order to assess the phase stability of the material with adsorbed water, and no compositional difference was apparent between the wet and the dry samples (fig. S17). Further, the Ni-BZCYYb anode is very stable under repeated electrochemical cycling: The terminal voltage of the cell was swept between OCV and 0.4 V at a rate of 10 mV/s for 1000 cycles with no appreciable change in peak power density (fig. S18). The remarkable ionic conductivity and stability suggest that BZCYYb is an attractive electrolyte or electrode component for low-temperature SOFCs. In addition, the material may also be used as a catalyst for reforming of hydrocarbon fuels and for removal of fuel gas contaminants such as sulfur.

References and Notes

1. S. C. Singhal, *Solid State Ion.* **135**, 305 (2000).
2. A. Atkinson *et al.*, *Nat. Mater.* **3**, 17 (2004).
3. M. Flytzani-Stephanopoulos, M. Sakbodin, Z. Wang, *Science* **312**, 1508 (2006).
4. E. P. Murray, T. Tsai, S. A. Barnett, *Nature* **400**, 649 (1999).
5. S. Park, J. M. Vohs, R. J. Gorte, *Nature* **404**, 265 (2000).
6. S. Tao, J. T. S. Irvine, *Nat. Mater.* **2**, 320 (2003).
7. Z. Zhan, S. A. Barnett, *Science* **308**, 844 (2005); published online 31 March 2005 (10.1126/science.1109213).
8. J. C. Ruiz-Morales *et al.*, *Nature* **439**, 568 (2006).

9. Y. H. Huang, R. I. Dass, Z. L. Xing, J. B. Goodenough, *Science* **312**, 254 (2006).
10. F. Z. Chen, S. W. Zha, J. Dong, M. L. Liu, *Solid State Ion.* **166**, 269 (2004).
11. O. A. Marina, N. L. Canfield, J. W. Stevenson, *Solid State Ion.* **149**, 21 (2002).
12. M. R. Pillai, I. Kim, D. M. Bierschenk, S. A. Barnett, *J. Power Sources* **185**, 1086 (2008).
13. K. D. Kreuer, *Annu. Rev. Mater. Res.* **33**, 333 (2003).
14. K. H. Ryu, S. M. Haile, *Solid State Ion.* **125**, 355 (1999).
15. Y. Yamazaki, P. Babilo, S. M. Haile, *Chem. Mater.* **20**, 6352 (2008).
16. K. Katahira, Y. Kohchi, T. Shimura, H. Iwahara, *Solid State Ion.* **138**, 91 (2000).
17. C. W. Tanner, A. V. Virkar, *J. Electrochem. Soc.* **143**, 1386 (1996).
18. C. D. Zuo, S. W. Zha, M. L. Liu, M. Hatano, M. Uchiyama, *Adv. Mater.* **18**, 3318 (2006).
19. L. Yang, C. D. Zuo, S. Z. Wang, Z. Cheng, M. L. Liu, *Adv. Mater.* **20**, 3280 (2008).
20. Z. Cheng, M. L. Liu, *Solid State Ion.* **178**, 925 (2007).
21. J. B. Hansen, J. Rostrup-Nielsen, in *Handbook of Fuel Cells—Fundamentals, Technology and Applications*, W. Vielstich, H. Yokokawa, H. A. Gasteiger, Eds. (Wiley, Chichester, UK, 2009), chap. 65.
22. J. H. Wang, M. L. Liu, *Electrochem. Commun.* **9**, 2212 (2007).
23. J. H. Wang, M. L. Liu, *J. Power Sources* **176**, 23 (2008).
24. V. Crupi, D. Majolino, P. Migliardo, V. Venuti, *J. Phys. Chem. A* **104**, 11000 (2000).
25. A. Anedda, C. M. Carbonaro, F. Clemente, R. Corpino, P. C. Ricci, *J. Phys. Chem. B* **107**, 13661 (2003).
26. B. Ratajska-Gadomska, W. Gadomski, *J. Chem. Phys.* **121**, 12583 (2004).
27. M. Mogensen, K. Kammer, *Annu. Rev. Mater. Res.* **33**, 321 (2003).
28. Supported by U.S. Department of Energy Basic Energy Science Catalysis Science Program grant DE-FG02-06ER15837.

Supporting Online Material

www.sciencemag.org/cgi/content/full/326/5949/126/DC1
Materials and Methods
SOM Text
Figs. S1 to S18
References

10 April 2009; accepted 7 August 2009
10.1126/science.1174811

Rapid Resurgence of Marine Productivity After the Cretaceous-Paleogene Mass Extinction

Julio Sepúlveda,^{1,2,*†} Jens E. Wendler,^{3‡} Roger E. Summons,⁴ Kai-Uwe Hinrichs^{1,2}

The course of the biotic recovery after the impact-related disruption of photosynthesis and mass extinction event at the Cretaceous-Paleogene boundary has been intensely debated. The resurgence of marine primary production in the aftermath remains poorly constrained because of the paucity of fossil records tracing primary producers that lack skeletons. Here we present a high-resolution record of geochemical variation in the remarkably thick Fiskeler (also known as the Fish Clay) boundary layer at Kulstirenden, Denmark. Converging evidence from the stable isotopes of carbon and nitrogen and abundances of algal steranes and bacterial hopanes indicates that algal primary productivity was strongly reduced for only a brief period of possibly less than a century after the impact, followed by a rapid resurgence of carbon fixation and ecological reorganization.

At the Cretaceous-Paleogene boundary (KPB) 65 million years ago, an asteroid impact was associated with mass extinction and widespread disruption of photosynthesis (1–3), possibly because of a reduction in incoming solar radiation caused by atmospheric debris

and sulfate aerosols (3, 4). Scenarios proposed for the immediate aftermath include a “Strangelove ocean,” where primary productivity was suppressed for a substantial interval of time (5), or an alternative “living ocean,” where there was little interruption of productivity and, instead, the

flux of organic matter from the surface to the deep ocean ceased in the postextinction ocean (2, 6). Model simulations suggest that the physical effects of reduced sunlight may have lasted no longer than a decade (4). It is assumed that pelagic ecosystems required up to ~3 million years to fully recuperate (2, 6), although continental margin ecosystems seemed to have recovered rather quickly (7, 8), possibly because opportunistic neritic species with benthic cysts or resting stages may

¹Organic Geochemistry Group, Department of Geosciences, and Center for Marine Environmental Sciences (MARUM), University of Bremen, 28334 Bremen, Germany. ²International Graduate College—Proxies in Earth History (EUROPROX), University of Bremen, 28334 Bremen, Germany. ³Research Group Geochronology—Basin Analysis, Department of Geosciences, University of Bremen, 28334 Bremen, Germany. ⁴Department of Earth, Atmospheric and Planetary Sciences, Massachusetts Institute of Technology (MIT), 45 Carleton Street, Cambridge, MA 02139, USA.

*To whom correspondence should be addressed. E-mail: juliosep@mit.edu

†Present address: Department of Earth, Atmospheric and Planetary Sciences, MIT, 45 Carleton Street E25-623, Cambridge, MA 02139, USA.

‡Present address: Institute of Earth Sciences, Faculty of Chemistry and Earth Sciences, Friedrich-Schiller-Universität Jena, Burgweg 11, 07749 Jena, Germany.



Supporting Online Material for

Enhanced Sulfur and Coking Tolerance of a Mixed Ion Conductor for SOFCs:



Lei Yang, Shizhong Wang, Kevin Blinn, Mingfei Liu, Ze Liu, Zhe Cheng, Meilin Liu*

*To whom correspondence should be addressed. E-mail: meilin.liu@mse.gatech.edu

Published 2 October 2009, *Science* **326**, 126 (2009)
DOI: 10.1126/science.1174811

This PDF file includes:

SOM Text

Figs. S1 to S18

Materials and Methods

References

1. Materials and methods

1.1 Electrolyte and electrode powder preparation

The compositions of the materials were $\text{BaZr}_{0.1}\text{Ce}_{0.7}\text{Y}_{0.2-x}\text{Yb}_x\text{O}_{3-\delta}$ ($x=0, 0.05, 0.1, 0.15, 0.2$). All powders were synthesized by a conventional solid state reaction method. Stoichiometric amounts of high-purity barium carbonate, zirconium oxide, cerium oxide, ytterbium oxide, and yttrium oxide powders (all from Aldrich Chemicals) were mixed by ball milling in ethanol for 48 h, followed by drying in an oven and calcination at 1100 °C in air for 10 h. The calcined powder was ball milled again, followed by another calcination at 1100°C in air for 10 h. For the conductivity measurement, the pre-calcined powders were then isostatically pressed into a disk at 274.6 MPa. The green disks had a diameter of 10 mm, with a typical thickness of 1 mm. The disks were then sintered at 1550 °C for 10 h in air (to achieve relative density > 96%). $\text{Sm}_{0.1}\text{Ce}_{0.9}\text{O}_{2-\delta}$ (SDC) powders were synthesized by a chemical co-precipitation process using corresponding metal nitrates as precursors and ammonium carbonate as the precipitation agent. After washing

and drying, the resultant powders were subsequently calcined at 800 °C for 2 h. $\text{Gd}_{0.1}\text{Ce}_{0.9}\text{O}_{2-\delta}$ (GDC) and $\text{Y}_{0.15}\text{Zr}_{0.85}\text{O}_{2-\delta}$ (YSZ) were obtained from TOSOH Co., while $\text{La}_{0.6}\text{Sr}_{0.4}\text{Co}_{0.2}\text{Fe}_{0.8}\text{O}_{3-\delta}$ (LSCF) and NiO powders were obtained from Fuel Cell Materials and Sigma-Aldrich.

1.2 Fabrication of test cells

The button cells with a configuration of Ni-BZCYYb|BZCYYb|cathode were fabricated as follows. First, a mixture of NiO and BZCYYb powder (weight ratio of 65:35) was pressed into pellets (~0.6 mm thick and 13 mm in diameter), followed by pre-firing at 800 °C for 2 h. Second, a thin layer of BZCYYb (~10 μm) was deposited on the anode support by a solution coating process followed by co-firing at 1400 °C for 5 h. Third, a BZCY-LSCF slurry was screen printed onto the top of the BZCYYb electrolyte and fired at 1000 °C for 2 h to form a porous cathode (~30 μm thick). The Ni-BZCYYb|SDC|LSCF cells were prepared by the same method. The LSCF cathode was fired at 1050 °C for 2 h. The SDC and LSCF layer thicknesses are about 20 and 30 μm, respectively. For the Ni-BZCYYb|YSZ|LSCF cells, a YSZ disk (150 μm thick and 20 mm in diameter) was fabricated by tape casting and firing at 1450 °C for 5 h. Next, a GDC buffer layer (5 μm) was screen-painted on both sides of the YSZ and fired at 1200 °C for 2 h. Finally, NiO-BZCYYb (analogous to NiO-GDC and NiO-YSZ) anodes and LSCF cathodes were screen-painted on the GDC buffer layers, followed by firing at 1050 °C for 2 h. For the cells with a BZCYYb infiltrated Ni-YSZ anode, solution infiltration (I-5) was used to deposit a thin layer of BZCYYb on the porous Ni-YSZ, followed by

calcination at 850 °C for 2 h to obtain a pure phase. The active electrode areas for all cells are 0.21 cm².

1.3 Electrochemical testing

For conductivity studies, platinum paste was applied to both sides of electrolyte disks and fired at 900°C for 30 min to form porous platinum electrodes. Two platinum wires were attached to each of the electrodes. The electrical conductivities were studied in dry and wet oxygen, H₂, argon, and 4% H₂ (balanced with argon) at different temperatures. The wet gases were prepared by passing the corresponding gases through a water bubbler at 25°C to bring in ~ 3 v% of water vapor.

For H₂S tests, each button cell was sealed on an alumina tube and heated up to 750°C in ambient air. Since H₂S can dissolve in water, a separate flow of N₂ was passed through a water bubbler to bring water vapor into the system. H₂S concentration was adjusted by mixing H₂ and a certified mixture gas containing 100 ppm H₂S in H₂ using two mass flow controllers. The flow rate was 30 mL/min. All fuel cells were first conditioned at a constant current density in clean H₂ to obtain steady state performance before switching to H₂S-contaminated H₂ (6-7).

For hydrocarbon testing, following reduction of anode in H₂, the cell was conditioned in H₂ as was just described, and then dry or wet C₃H₈ with a flow rate of 2 mL/min (passing through a water bubbler at room temperature) was fed into the cell at 750 °C.

1.4 Other Characterization

X-ray diffraction with $\text{CuK}\alpha$ radiation (Philips, PW-1800) and Raman spectroscopy with a 514 nm excitation source (Renishaw, Raman System 2000) were used to analyze crystal structure and phase composition. Raman was also used to probe water adsorbed on sample surfaces. The microstructures of fuel cells before and after testing were revealed using a scanning electron microscope (SEM; LEO 1530) equipped with energy dispersive x-ray spectroscopy (EDS). The stability of BZCYYb powders was tested by exposing materials to H_2 containing 50 v% H_2O (passed through a water bubbler at 85°C) and 50 v% CO_2 . The composition of the inlet and outlet gas mixture was monitored online by mass spectrometer (MS, Hiden HPR 20) at room temperature. All standard electrochemical experiments were performed using a Solartron 1286 electrochemical interface and a Solartron 1255 HF frequency response analyzer.

2. Supporting text

2.1 General Properties of $\text{BaZr}_{0.1}\text{Ce}_{0.7}\text{Y}_{0.2-x}\text{Yb}_x\text{O}_{3-\delta}$ ($x=0-0.2$)

Fig. S1 shows XRD patterns of various Yb-doped $\text{BaZr}_{0.1}\text{Ce}_{0.7}\text{Y}_{0.2}\text{O}_{3-\delta}$. A pattern for a pure perovskite resembling that of BaCeO_3 can be observed. It is clear that Yb has replaced Y and has been doped into the lattice of $\text{BaZr}_{0.1}\text{Ce}_{0.7}\text{Y}_{0.2}\text{O}_{3-\delta}$ properly. Furthermore, XRD patterns of the materials did not change after conductivity measurements in dry and wet argon, oxygen, and hydrogen, suggesting that the samples are quite stable over a wide range of oxygen partial pressures.

Fig. S2 shows the conductivities of $\text{BaZr}_{0.1}\text{Ce}_{0.7}\text{Y}_{0.2-x}\text{Yb}_x\text{O}_{3-\delta}$ ($x=0-0.2$) in wet oxygen. The conductivities measured at different temperatures seem to have similar

dependence on Yb concentration. The conductivities increase quickly with increasing Yb concentration, reaching a maximum at ~10%. With any further increase in the concentration of Yb dopant, the conductivities decreased slightly. However, the conductivities in $\text{BaZr}_{0.1}\text{Ce}_{0.7}\text{Yb}_{0.2}\text{O}_{3-\delta}$ are still higher than those in $\text{BaZr}_{0.1}\text{Ce}_{0.7}\text{Y}_{0.2}\text{O}_{3-\delta}$. It is interesting to see that the barium zirconate-cerate solid solution containing multiple dopants has a higher conductivity than one containing a single dopant, which could herald a new method for the design of high-conductivity proton conductors.

Fig. S3 shows the open circuit voltages, together with the Nernst potentials, for a cell based on a BZCYYb electrolyte membrane at different temperatures with wet H_2 (~ 3 v% H_2O) as fuel and air as oxidant. The electronic transference number varies from ~0.02 at 500°C to ~0.1 at 750°C , suggesting that the electronic conduction is relatively insignificant at low temperatures.

Fig. S4 shows the open cell voltages (OCVs) of two cells with different anodes: Ni-BZCYYb and Ni-BZCY. The cell with a Ni-BZCYYb anode displayed higher and more stable OCVs than the cell with a Ni-BZCY anode, suggesting that BZCYYb has much-improved ability for hydrocarbon reformation.

Fig. S5 shows the morphologies of a typical Ni-BZCYYb | BZCYYb | BZCY-LSCF cell as fabricated (before NiO was reduced to Ni). The BZCYYb electrolyte is ~ 10 μm thick and adhered well to the anode support, indicating that our solution coating method can produce a thin and dense BZCYYb electrolyte that requires a relatively low sintering temperature. The average grain size is relatively large (~15 μm), which could effectively reduce grain boundary resistance.

Fig. S6 shows the current-voltage characteristics and the corresponding power density for a fuel cell based on a Ni-BZCYYb anode, a BZCYYb electrolyte, and a BZCY-LSCF composite cathode at 650 °C, demonstrating a peak power density is ~660 mW/cm².

2.2 Stability of Ni-BZCYYb anodes in H₂S-contaminated H₂ and C₃H₈

Fig. S7 shows the performance of a cell with a configuration of BZCYYb/Ni-YSZ | YSZ | LSCF operated in wet hydrogen contaminated with 10 ppm H₂S. The Ni-YSZ anode was coated with a thin layer of BZCYYb using a solution infiltration process. This cell demonstrated that the state-of-the-art fuel cells based on YSZ, Ni-YSZ|YSZ|LSCF, can be readily modified by a thin film coating of BZCYYb to enhance the tolerance to sulfur poisoning. Further, the cell showed a stable power output for 1000 h, implying that BZCYYb exhibits considerable stability for long-term sulfur tolerance.

Fig. S8 shows the performance of a Ni-BZCYYb | SDC | LSCF cell operated at a constant current density of 700 mA/cm² at 750 °C when the fuel was switched from wet hydrogen to wet hydrogen contaminated with 30 ppm H₂S, indicating that sulfur poisoning can be fully suppressed in the presence of a small amount of water. After the 200 h operation, the Ni-BZCYYb anode surface was examined by EDS under SEM, but there was no sulfur detected.

We used electron microscopy and Raman spectroscopy to determine if carbon had deposited in the anode structure after exposure to dry and wet propane under open circuit conditions, the most severe conditions for carbon deposition (since the operation of the cell will produce water and CO₂ at the anode, thus increasing the steam to carbon ratio

and the probability of reformation). If coking is absent at OCV, it would be less likely to occur during cell operation. Fig. S9 shows a typical morphology of Ni-BZCYYb anode and EDS spectrum collected from a Ni area, suggesting that Ba is present in the Ni area. Apparently, the Ni grains had been contaminated by BZCYYb. XPS analysis of the surface of Ni grains also confirms that Ba was present on the surface. The contamination of Ni surface by BZCYYb most likely happened during the co-firing of BZCYYb and NiO (at 1400°C for 5 hours). In all likelihood, the spreading of elements from BZCYYb to the surface of NiO grains during co-firing resulted in a surface that has enhanced resistance to coking. While it is certain that the Ni surface became contaminated by BZCYYb, the detailed structure of this contaminated Ni surface is still unknown. *In situ* surface analysis techniques must be used to characterize the surface composition and structure under SOFC operating conditions because *ex situ* surface characterization may not be reliable; the surface composition and structure may change as a functional cell is cooled down (from 750°C in the fuel to room temperature in air) to prepare samples for *ex situ* analysis such as electron microscopy and spectroscopy in vacuum.

Since Raman is very sensitive to trace amounts of carbon (which may not be observable under SEM examination), we used Raman spectroscopy to probe and map the presence of any carbon on a large area of an anode surface after exposure to propane. Fig. S10 shows some typical Raman spectra collected from Ni-BZCYYb anodes after exposure to wet and dry propane under open circuit conditions. While the disordered and graphitic carbon peaks (near 1340 cm^{-1} and 1580 cm^{-1} , respectively) (8) were readily observable from the anode exposed to dry propane (Fig. S10a), they were largely absent from the spectra collected from the same anode surface after exposure to wet (~3 v%

H₂O) propane (Fig. S10b). Out of 100 spectra collected from 100 points uniformly distributed in a rectangular mesh covering an area of 80 μm x 60 μm, only 42 spectra show a trace amount of carbon, and are comparable to Fig. S10c, an indication of minimal carbon deposition.

Fig. S11 shows that the OCVs of a cell with a Ni-GDC anode and YSZ electrolyte decreased rapidly upon exposure to wet (3 v% water) propane, while the OCVs of a cell with a Ni-BZCYYb anode was very stable under the same conditions, an indication of remarkable tolerance to coking of BZCYYb over GDC. The strong adsorption of water on the surface of BZCYYb, the TPB, and the contaminated Ni surface may dramatically change the local composition of the fuel in equilibrium with these surface sites on the anode. While the average steam to carbon ratio (S/C) for the incoming wet (~3v % H₂O) propane in the gas phase is about 1 to 97, this ratio could be much greater on the anode surface because of the strong adsorption of water, possibly approaching the needed S/C ratio to avoid coking (about 1:1) under open circuit conditions.

Fig. S12 shows open circuit voltages and power output at a constant current density of 300 mA/cm² for a cell with a configuration of Ni-BZCYYb |YSZ | LSCF when wet (~3 v% steam) propane was used as fuel and air as oxidant. It demonstrated stable OCV and sustained power output for over 100 h when wet propane was used as fuel. The outlet gas from this cell under steady state operation was analyzed using mass spectrometry, as shown in Fig. S13. Due to the instrumental limitations, it is not possible to determine the relative contributions of the fragments [CO]⁺ and [C₂H₄]⁺ to the mass signal at $m/z = 28$. However, our analysis of oxygen mass balance suggests that the ratio of CO to C₂H₄ is relative small. At an operating current of 63 mA (= 0.21 cm² ×300

mA/cm²), the oxygen flux going through the electrolyte to the anode was $\sim 3.21 \times 10^{-7}$ mol/s or 0.431 mL/min. Since the concentrations of H₂O and CO₂ in the outlet gas mixture were 3.58 v% and 2.34 v%, respectively, the concentration of CO in the outlet gas should be ~ 2.65 v%, considering that ~ 3 v% of water was fed with propane in the inlet gas. Analysis of carbon mass balance suggests that the mass of carbon for the inlet gas is slightly larger than that for the outlet gas. This is reasonable since small amount of carbon deposits were observed on the gas feeding tube walls after operation. It appears that a large fraction of C₃H₈ was converted to C₂H₄ and CH₄, but the details about cracking, reformation, and electrochemical oxidation during fuel cell operation are still unknown. However, it is certain that the *in situ* reforming and electrochemical oxidation are sufficiently fast to avoid carbon buildup at the anode.

Fig. S14 shows the morphologies of a Ni-BZCYYb | SDC | LSCF cell before and after operation in dry propane at a constant current density of 600 mA/cm² for 24 hours. It is seen that the Ni-BZCYYb anode exhibit fine uniform microstructures and that no carbon deposits blocked the pores. Further, the anode adheres well to the electrolyte.

3.3 Chemical and Electrochemical Stability of BZCYYb in H₂O, CO₂, and H₂S

Fig. S15 shows XRD patterns of BZCYYb powders before and after exposure to H₂ with 50 vol % CO₂ and H₂ with 50 % H₂O at 750 °C for 300 h. Contrary to decomposition that is normally seen in doped BaCeO₃, it can be observed that the structure of BZCYYb is stable in an atmosphere containing H₂O or CO₂. The partial substitution of Ce by Zr did indeed increase the chemical stability of this material (9-11). Additionally, Y and Yb are further shown as stable dopants for cerate system (12).

Fig. S16 indicates XRD patterns of BZCYYb powders before and after exposure to 50 ppm H₂S-contaminated H₂. It was shown that no chemical reactions occur between BZCYYb and H₂S at 50 ppm.

Fig. S17 shows a characteristic Raman spectrum for BZCYYb, which is similar to that of BaCeO₃. The most intense signals, which are found in the 275-350 cm⁻¹ range, are produced by Ce-O stretching in the structure (13). The Ce-O vibrations are generally observed in the 300-375 cm⁻¹ range for BaCeO₃ spectra. Thus, the shift in the Ce-O range in the BZCYYb spectrum is most likely an effect of the dopants in BZCYYb. No difference in composition is observable between wet and dry BZCYYb, so the bulk phase remains unchanged between these conditions.

To evaluate the electrochemical stability of Ni-BZCYYb anode, we first ran the cells for repeated power cycles from open circuit voltage (OCV) to 0.4 V and back to OCV. The potential sweeping rate was 10 mV/s. The Ni-BZCYYb anode is electrochemically stable under the testing conditions, as demonstrated by the cycling data shown in Fig. S18.

Supporting figures and legends

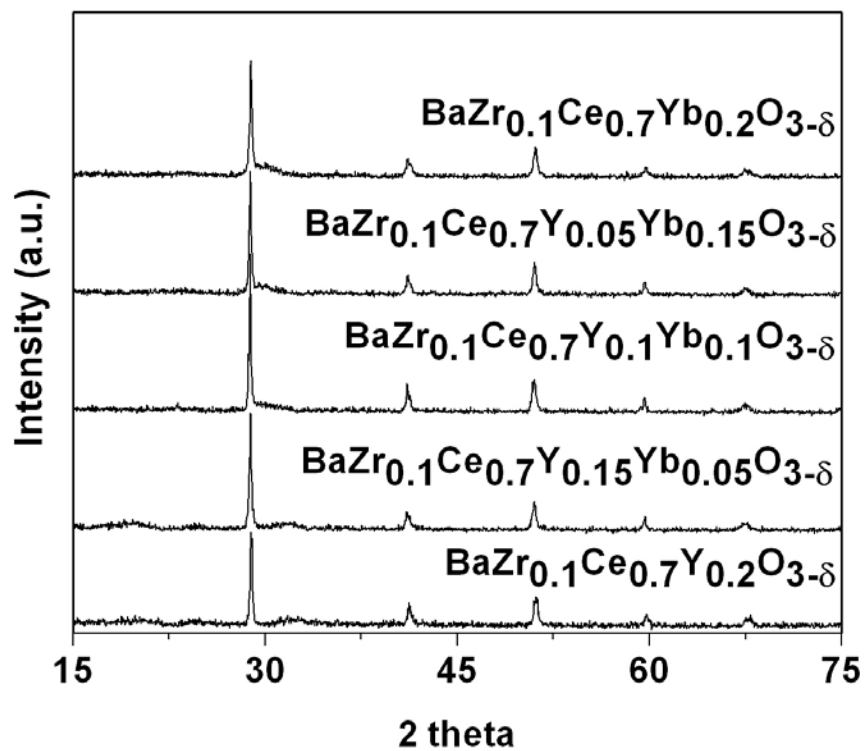


Fig. S1. XRD patterns of BaZr_{0.1}Ce_{0.7}Y_{0.2-x}Yb_xO_{3-δ}(x=0-0.2) powders.

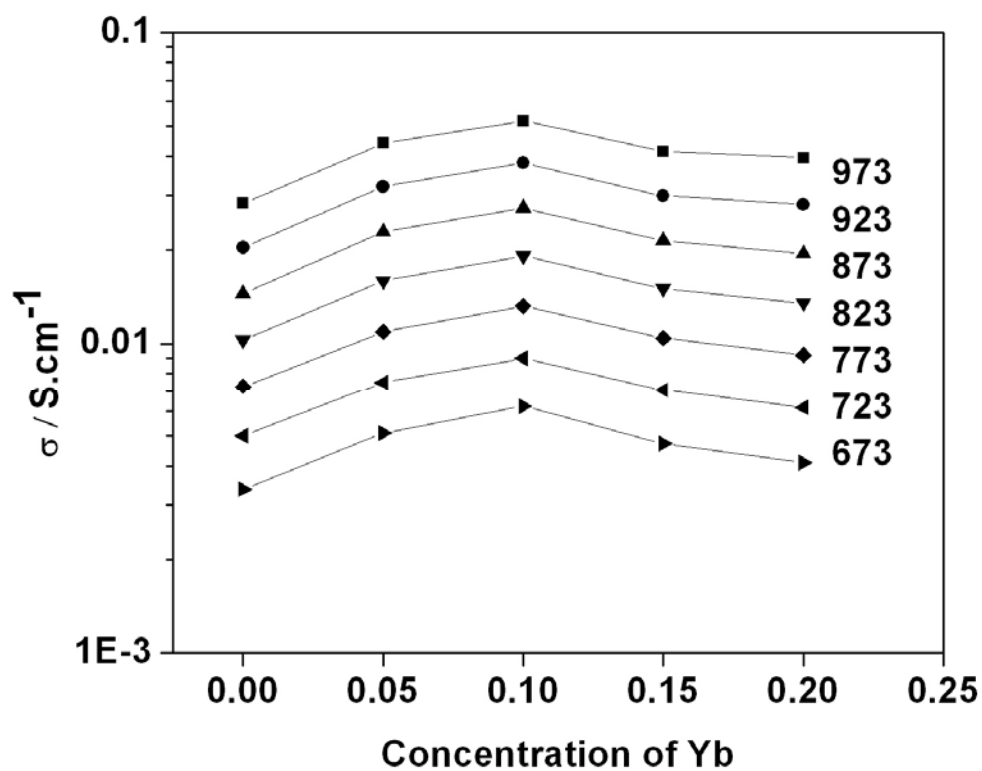


Fig. S2. The conductivities of $\text{BaZr}_{0.1}\text{Ce}_{0.7}\text{Y}_{0.2-x}\text{Yb}_x\text{O}_{3-\delta}$ ($x=0-0.2$) in wet oxygen at different temperatures as a function of the concentration of Yb. The number by each set of data represents the absolute temperature at which the conductivity was measured.

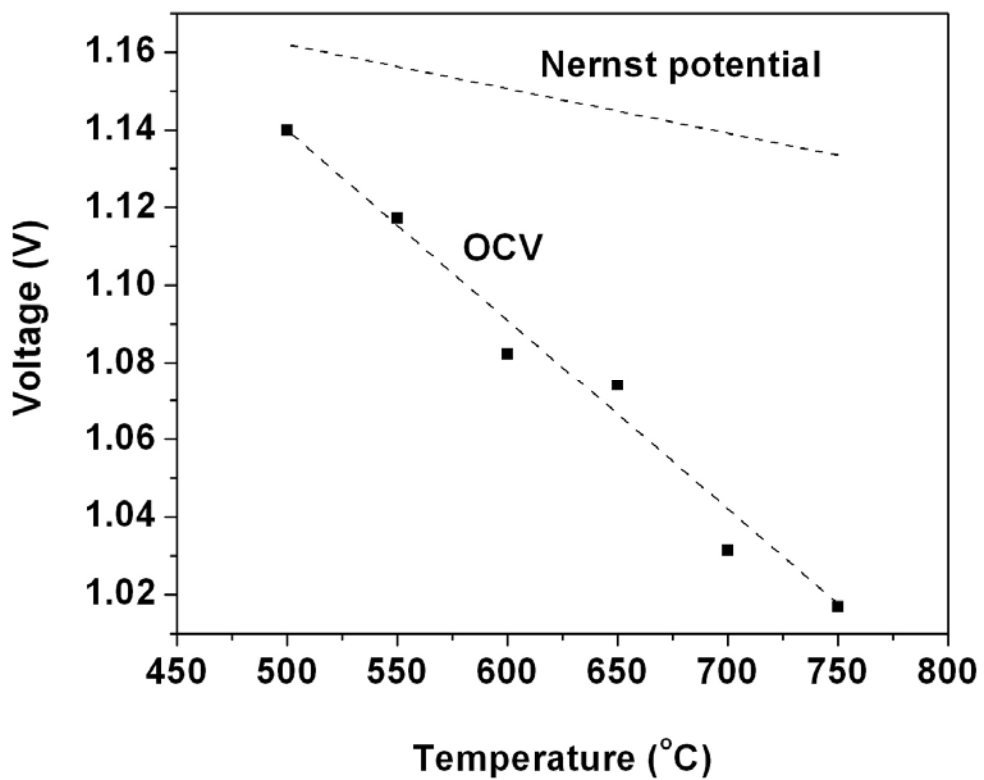


Fig. S3. Open circuit voltages (OCV) for a cell with a configuration of Pt | BZCYYb | Pt with wet H₂ (~ 3 v% H₂O) as fuel and air as oxidant.

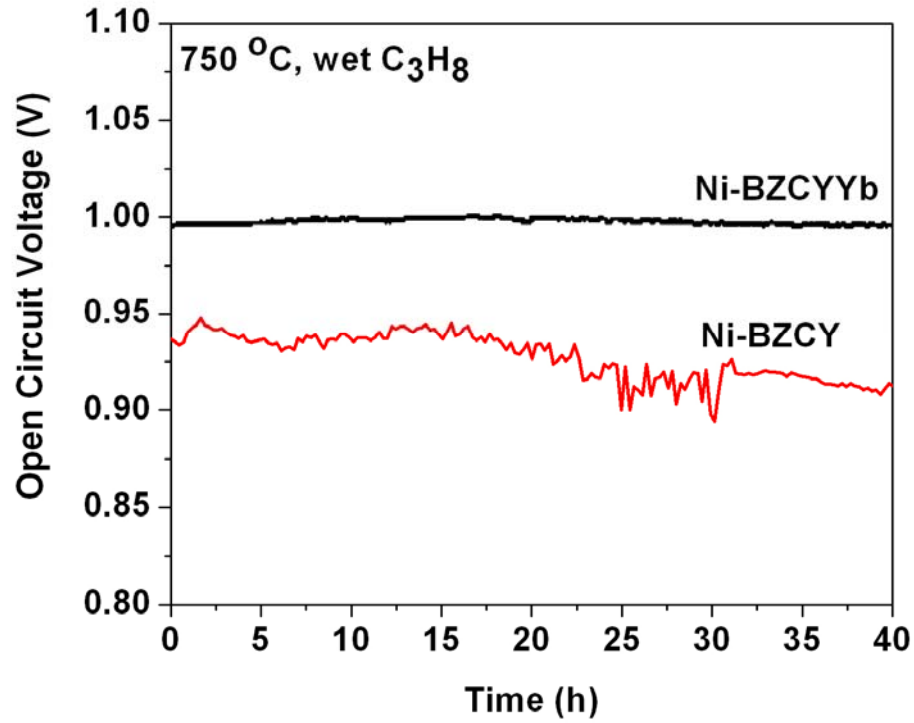


Fig. S4. Open circuit voltages measured at 750°C for cells with configurations of Ni-BZCYYb | YSZ | LSCF and Ni-BZCY | YSZ | LSCF with wet propane as the fuel and stationary air as oxidant.

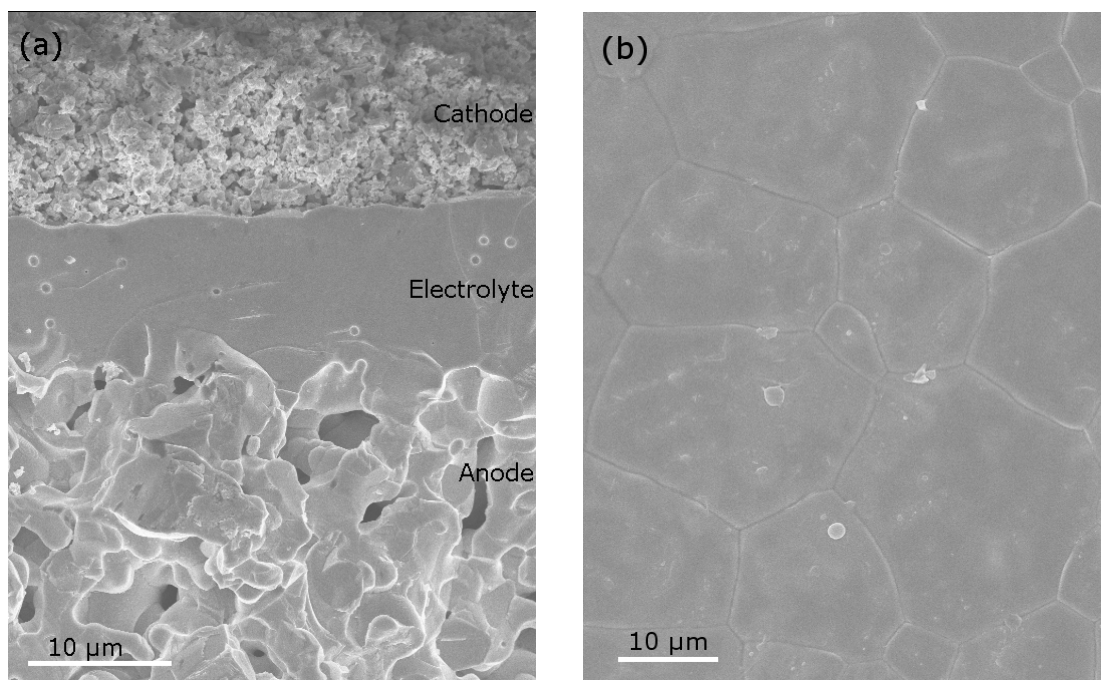


Fig. S5. (a) A cross-sectional view of a cell with a configuration of Ni-BZCYYb | BZCYYb | BZCY-LSCF and (b) a surface view of the BZCYYb electrolyte as fabricated using a solution coating process.

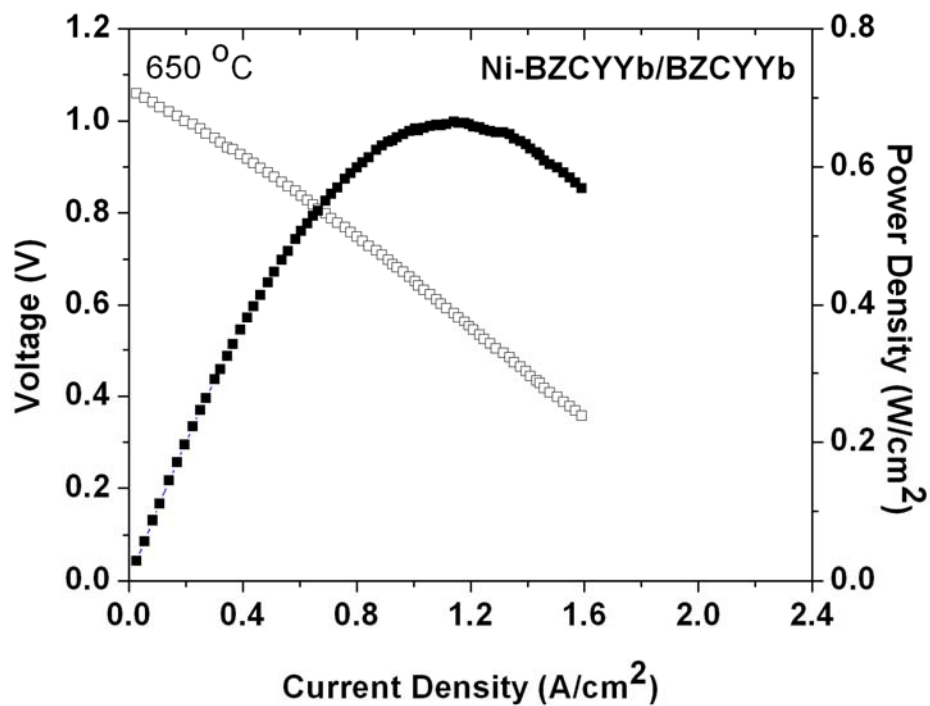


Fig. S6. Typical current-voltage characteristics and the corresponding power densities measured at 650°C for a cell with a configuration of Ni-BZCYYb | BZCYYb | BZCY-LSCF when ambient air was used as oxidant and wet hydrogen as fuel.

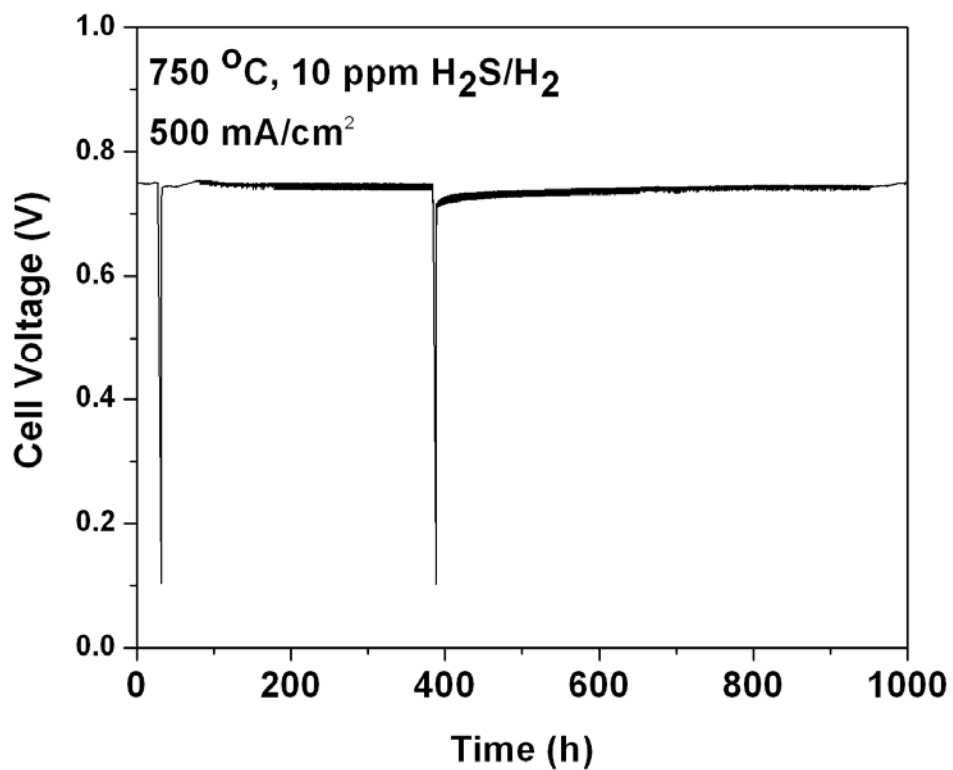


Fig. S7. Terminal voltage for a cell with a configuration of BZCYYb/Ni-YSZ | YSZ | LSCF operated at 500 mA/cm² in wet hydrogen containing 10 ppm H₂S at 750 °C. The Ni-YSZ anode was infiltrated with a BZCYYb solution to introduce a thin coating of BZCYYb on the surface of the Ni-YSZ anode.

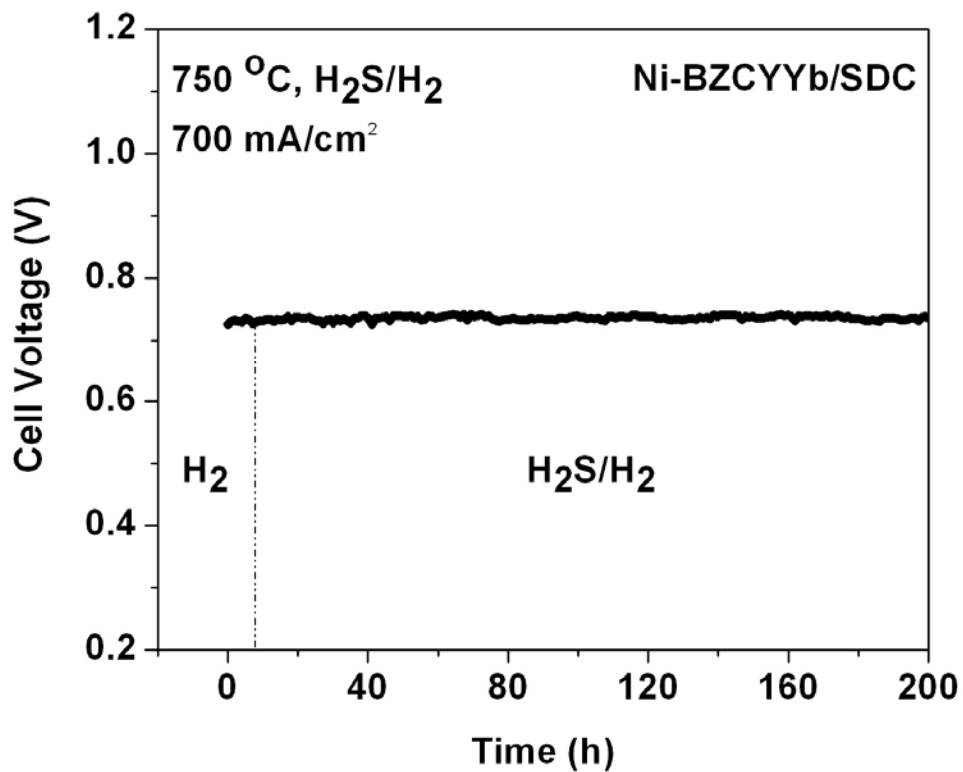


Fig. S8. Terminal voltage for a Ni-BZCYYb | SDC | LSCF cell operated at a constant current density of 700 mA/cm² in wet H₂ and wet H₂ containing 30 ppm H₂S at 750 °C. The fuel was switched to wet H₂ containing 30 ppm H₂S after a few hours operation in wet H₂.

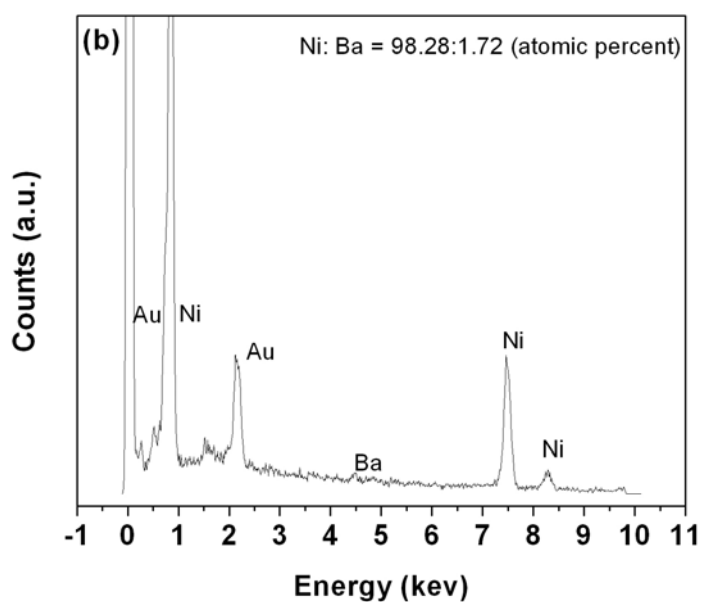
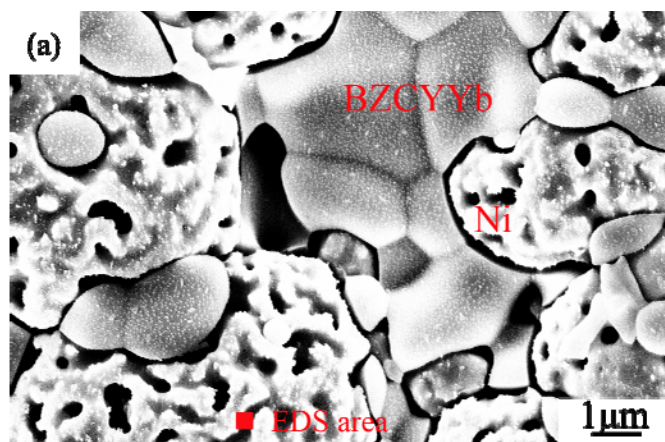


Fig. S9. (a) Surface morphology of Ni-BZCYyb anode in a cell with a configuration of Ni-BZCYyb | YSZ | LSCF (b) A typical EDS spectrum collected from the Ni grain area in a Ni-BZCYyb composite anode. (The spectrum also shows Au, which is from the Au coating on the sample surface to minimize charging during SEM analysis).

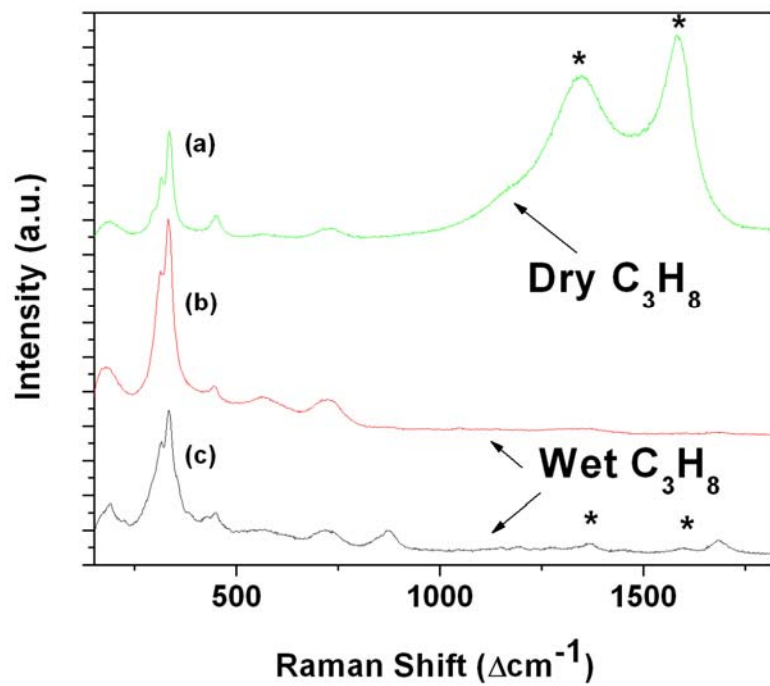


Fig. S10. Raman spectra collected from Ni-BZCYYb anode in a cell with a configuration of Ni-BZCYYb | YSZ | LSCF after exposure to (a) dry and (b), (c) wet propane at 750°C for 3 hours under OCV condition.

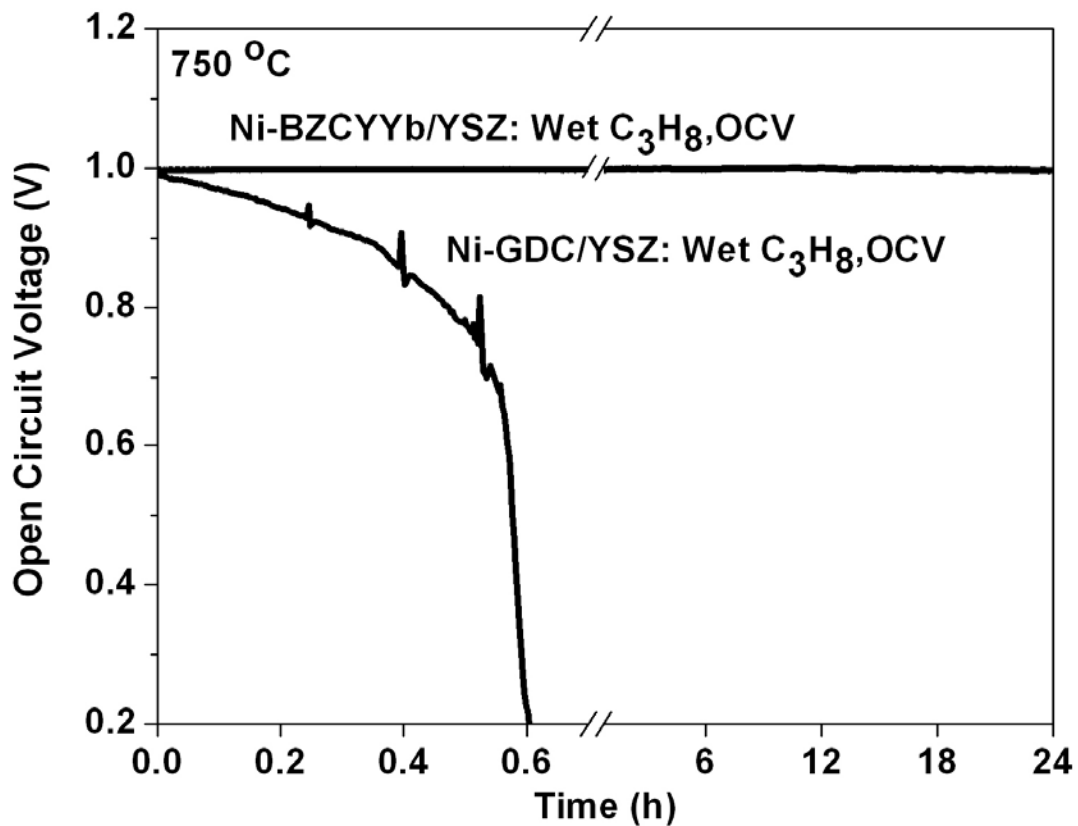


Fig. S11. Open circuit voltages measured at 750°C for cells with configurations of Ni-BZCYYb | YSZ | LSCF and Ni-GDC | YSZ | LSCF with wet propane as the fuel and stationary air as oxidant.

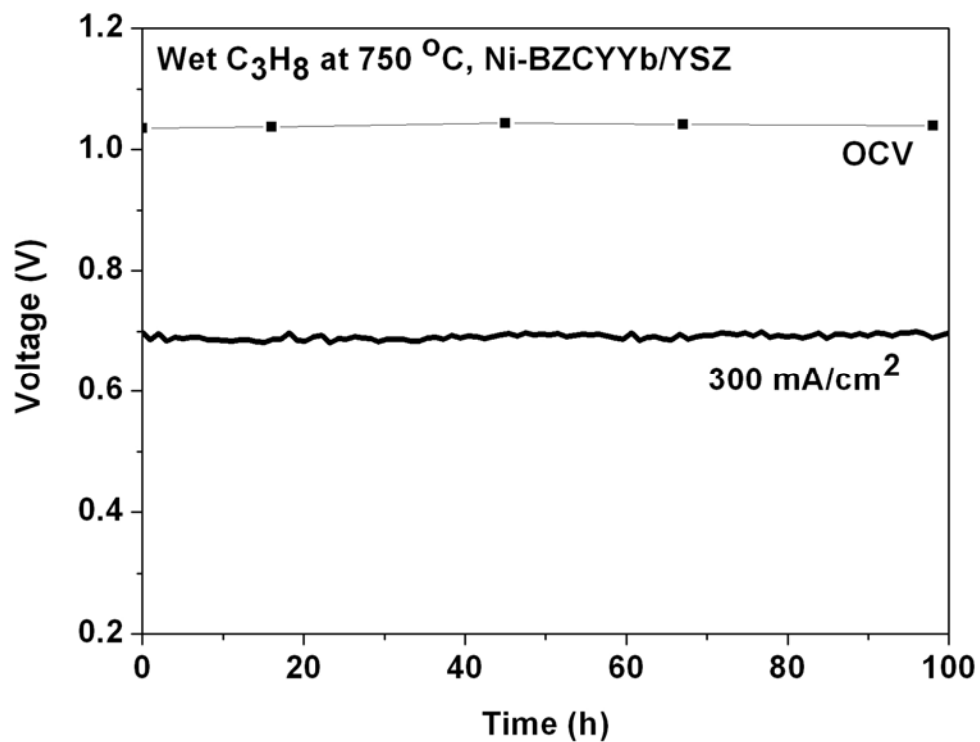


Fig. S12. Terminal voltages measured at a current density of 300 mA/cm² and OCVs (intermittently monitored) at 750°C for a cell with a configuration of Ni-BZCYYb |YSZ| LSCF with wet (with ~3 v% H₂O) propane as fuel and stationary air as oxidant.

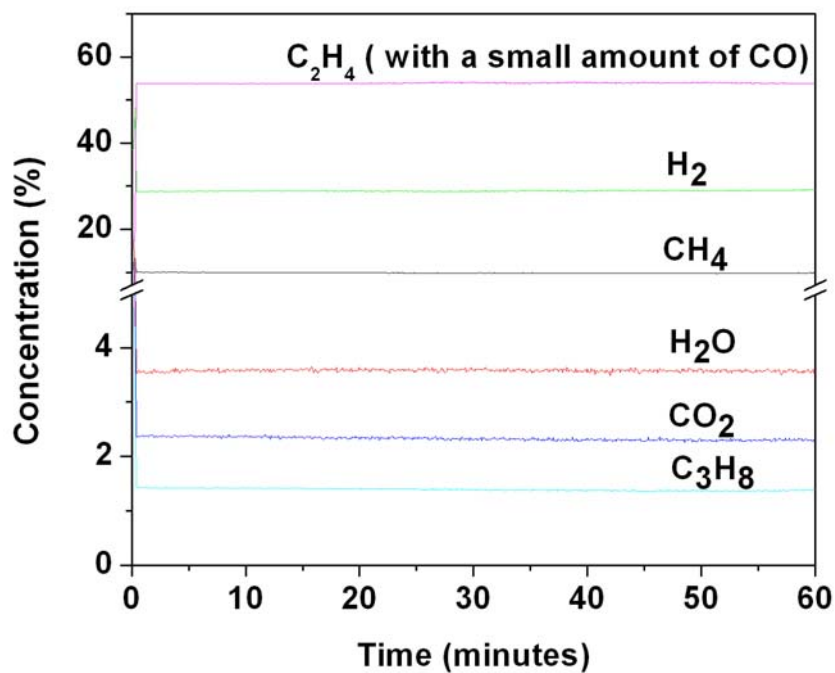


Fig. S13. A typical concentration profile of the outlet gas mixture monitored by mass spectrometer during operation of a Ni-BZCYYb | YSZ | LSCF cell (electrode area 0.21 cm^2) at a constant current density of 300 mA/cm^2 in wet C_3H_8 ($\sim 3 \text{ v\% H}_2O$). The flow rates for the inlet and outlet gas are 2.0 and 4.5 mL/min , respectively.

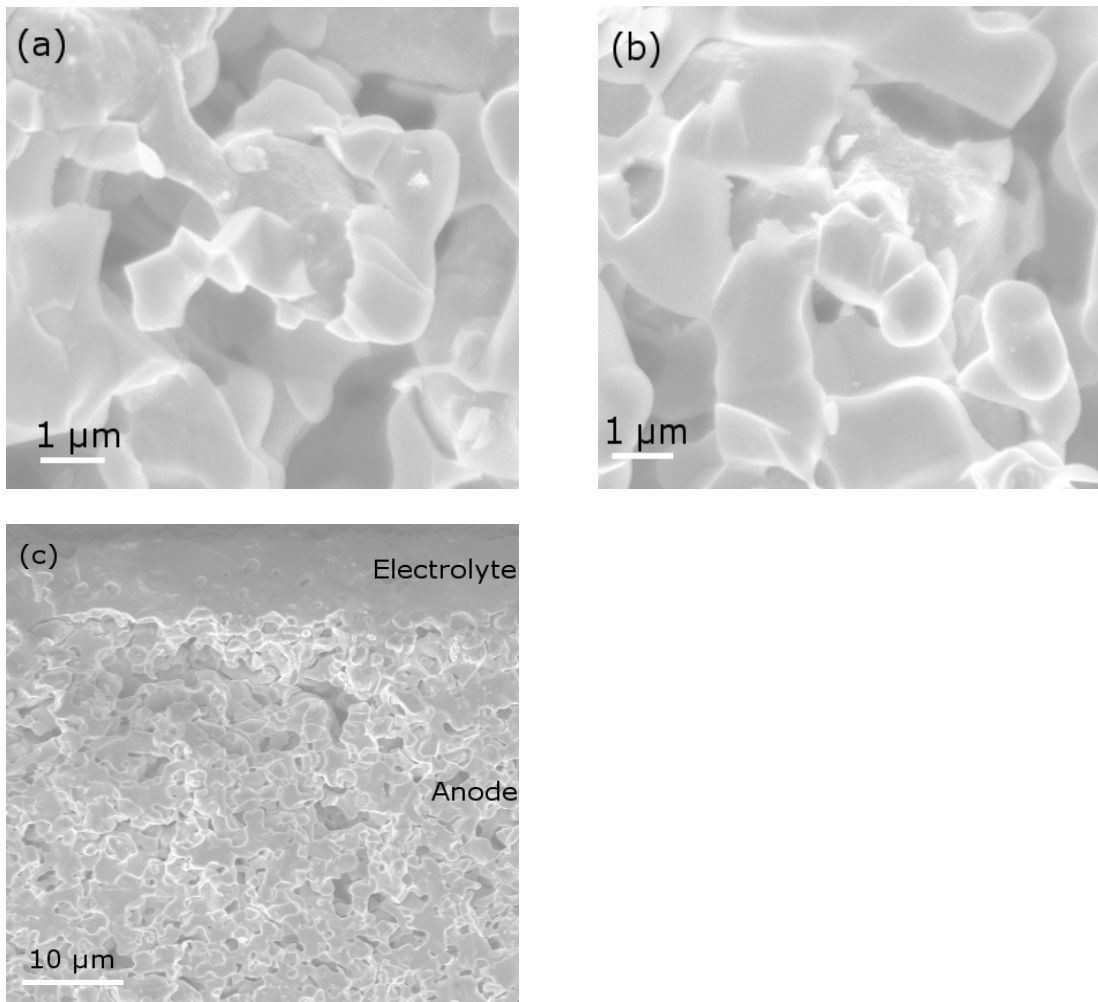


Fig. S14. Morphologies of the Ni-BZCYYb anode of a Ni-BZCYYb |SDC| LSCF cell (a) before and (b) after operation in dry propane at a constant current density of 600 mA/cm² for 24 hours. (c) a cross-sectional view of the cell after operation showing the anode/electrolyte interface.

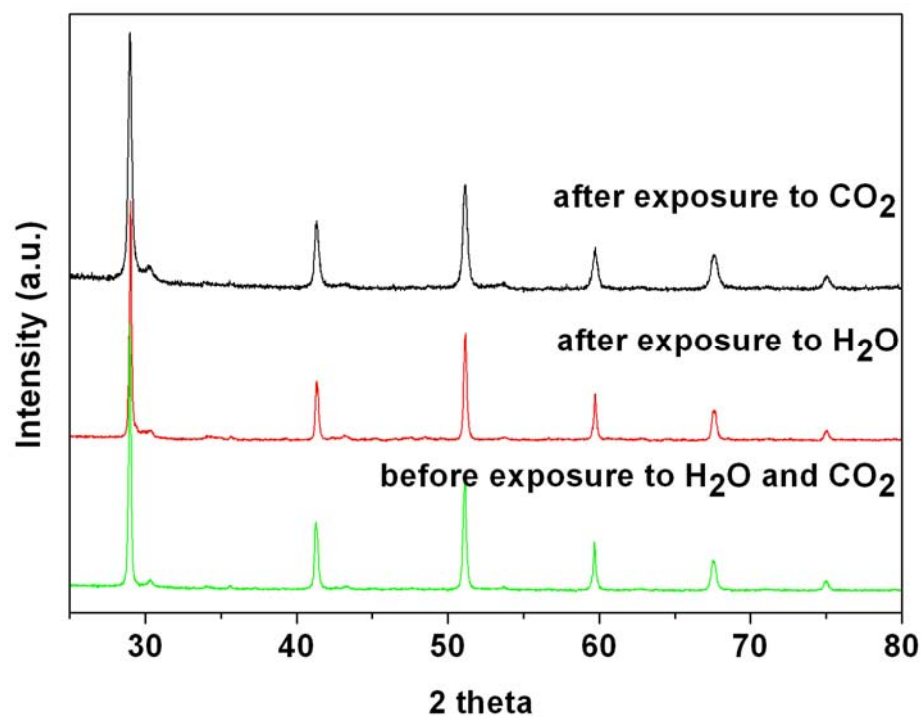


Fig. S15. XRD patterns for $\text{BaZr}_{0.1}\text{Ce}_{0.7}\text{Y}_{0.1}\text{Yb}_{0.1}\text{O}_{3-\delta}$ powders before and after exposure to H_2 with 50 vol % H_2O or H_2 with 50 vol % CO_2 at 750°C for 300 h.

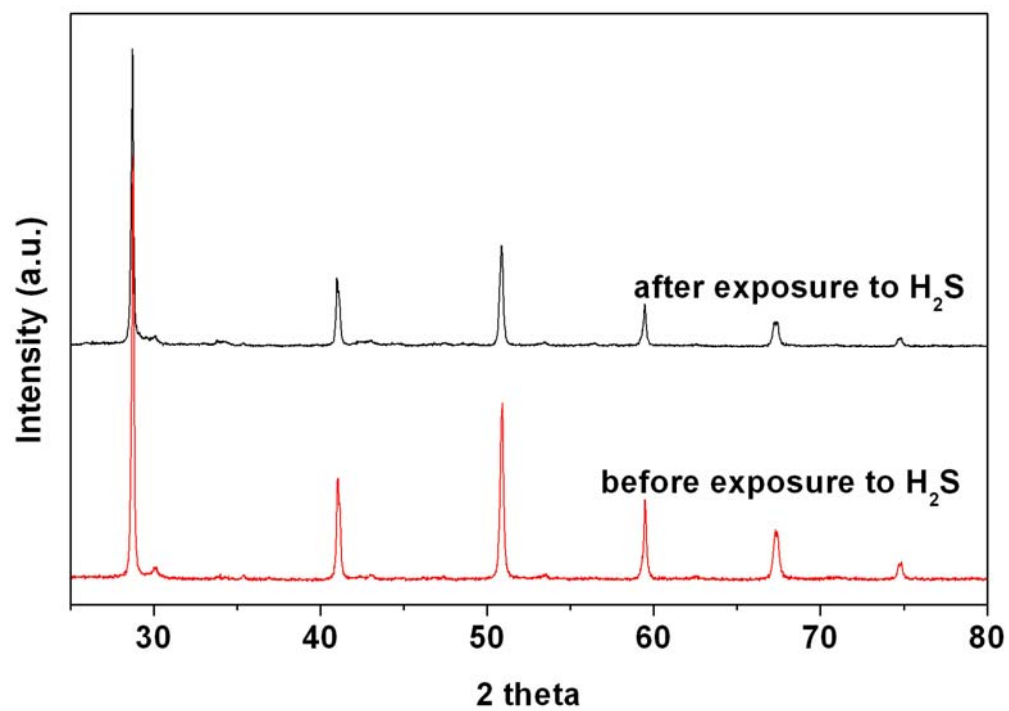


Fig. S16. XRD patterns for BaZr_{0.1}Ce_{0.7}Y_{0.1}Yb_{0.1}O_{3-δ} powders before and after exposure to 50 ppm H₂S/H₂ at 750 °C for 50 h.

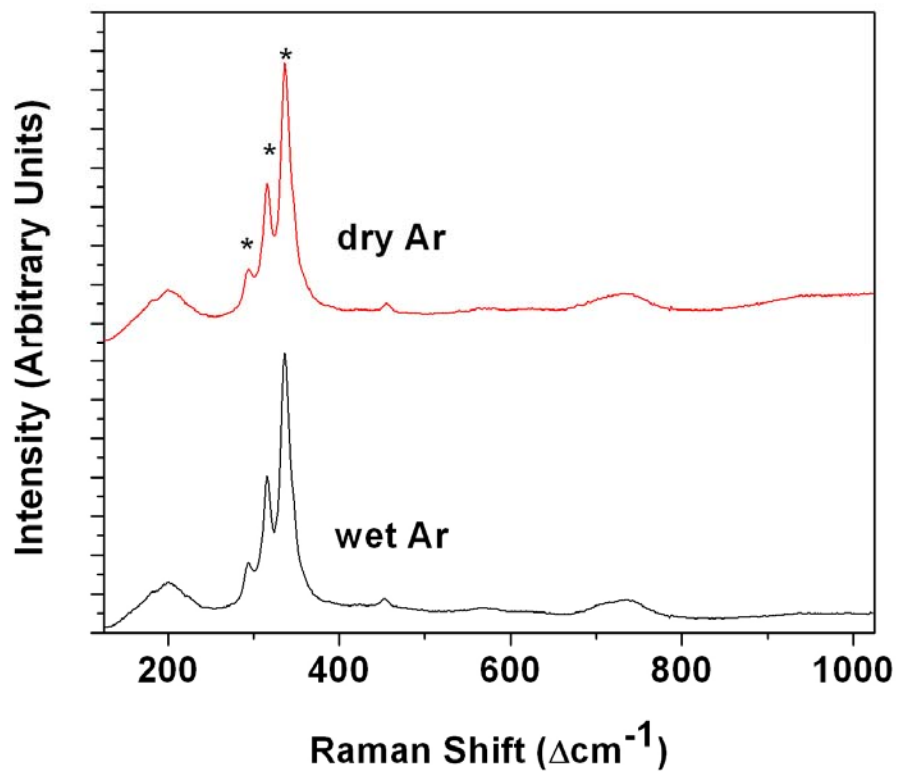


Fig. S17. Raman spectra collected in-situ at room temperature (25 °C) under wet and dry conditions.

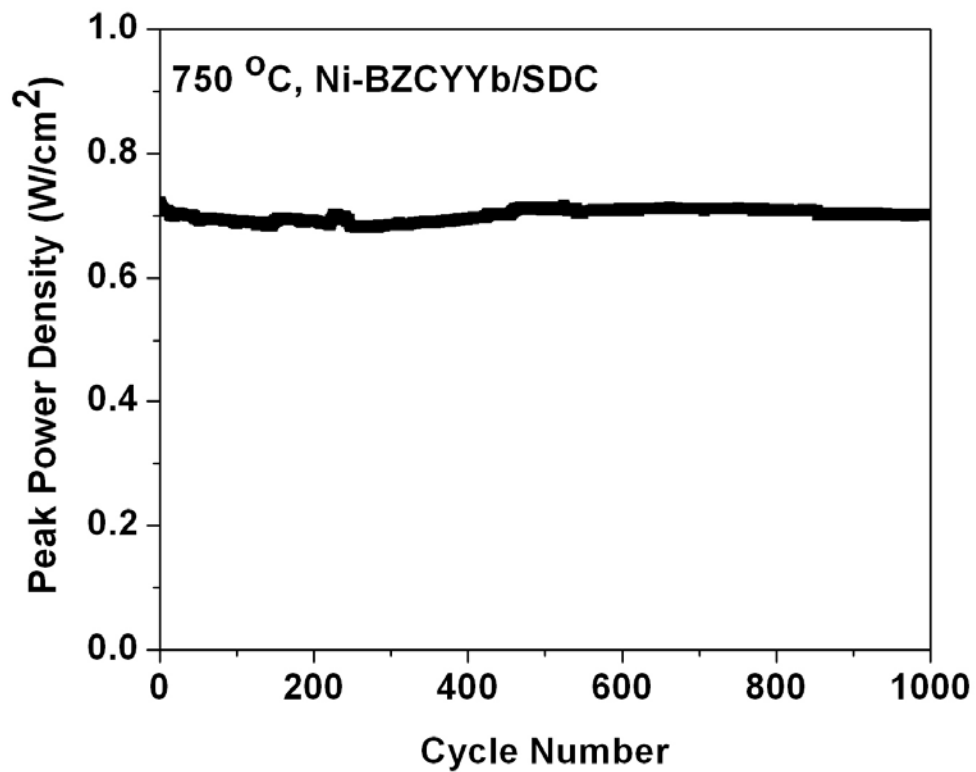


Fig. S18. The peak power density versus cycle number for a Ni-BZCYYb | SDC | LSCF cell at 750 °C in wet H₂. Repeated power cycles from open circuit voltage (OCV) to a terminal voltage of 0.4 V and back to OCV.

Supporting references

- S1. T. Z. Sholklapper, H. Kurokawa, C. P. Jacobson, S. J. Visco, L. C. De Jonghe, *Nano Lett.* **7**, 2136 (2007)
- S2. J. M. Vohs, R. J. Gorte, *Adv. Mater.* **21**, 943 (2009)
- S3. S. P. Jiang, *Mater. Sci. Eng. A-Struct.* **418**, 199 (2006)
- S4. M. Shah, J. D. Nicholas, S. A. Barnett, *Electrochem. Commun.* **11**, 2 (2009)
- S5. C. Torres-Garibay, D. Kovar, A. Manthiram, *J. Power Sources* **187**, 480 (2009).
- S6. Y. Matsuzaki, I. Yasuda, *Solid State Ionics* **132**, 261 (2000).
- S7. M. Y. Gong , X. B. Liu , J. Trembly , C. Johnson, *J. Power Sources* **168**, 289 (2007).
- S8. M. Pomfret, J. C. Owrutsky, R. Walker, *Anal. Chem.* **79**, 2367 (2007)
- S9. K. H. Ryu, S. M. Haile, *Solid State Ionics* **125**, 355 (1999).
- S10. S. Wienstroer, H.D. Wiemhofer, *Solid State Ionics* **101**, 1113 (1997).
- S11 C. D. Savaniu, J. Canales-Vazquez, J. T. S. Irvine, *J. Mater. Chem.* **15**, 598 (2005)
- S12 H. Matsumoto , Y. Kawasaki , N. Ito , M. Enoki , T. Ishihara, *Electrochem. Solid-State Lett.* **10**, B77 (2007)
- S13. T. Scherban, R. Villeneuve, L. Abello, G. Lucazeau, *J. Raman Spectrosc.* **24**, 805 (1993).